materials

MDPI

Article

Experimental and Theoretical Study of Ultra-Hard $AlMgB_{14}$-TiB_2 Composites: Structure, Hardness and Self-Lubricity

Pavel Nikitin [1], Ilya Zhukov [1,*], Dmitrii Tkachev [1], Yurii Abzaev [2], Ekaterina Marchenko [3] and Alexander Vorozhtsov [1]

[1] Laboratory of Metallurgy Nanotechnologies, National Research Tomsk State University, Lenin Avenue, 36, 634050 Tomsk, Russia
[2] Department of Higher Mathematics, Tomsk State University of Architecture and Building, Solyanaya Sq., 2, Building 2, 634003 Tomsk, Russia
[3] Laboratory of Superelastic Biointerfaces, National Research Tomsk State University, Lenin Avenue, 36, 634050 Tomsk, Russia
* Correspondence: gofra930@gmail.com

Abstract: It is known that the presence of oxygen phases in hard materials leads to an undesirable decrease in the mechanical properties. In materials based on $AlMgB_{14}$, the main oxygen impurity is spinel $MgAl_2O_4$; it significantly reduces the hardness of $AlMgB_{14}$ and its formation during sintering is inevitable. In this work, the ultra-hard spark plasma sintered (SPSed) $AlMgB_{14}$-TiB_2 composite material was fabricated from the $AlMgB_{14}$-TiB_2 precursor obtained by self-propagating high-temperature synthesis (SHS). Due to the high synthesis temperatures, the main oxygen phase in the obtained composite was $Al_4B_2O_9$ instead of spinel $MgAl_2O_4$. It was found that the obtained composite has excellent mechanical properties. The maximum hardness of the sample is 44.1 GPa. The presence of oxygen in the form of the $Al_4B_2O_9$ phase led to unexpected results: the friction coefficient of the obtained $AlMgB_{14}$-TiB_2 composite under dry conditions against the Al_2O_3 counter-specimen is approximately four times lower than the friction coefficient of pure ceramic $AlMgB_{14}$ (0.18 against 0.7, respectively). Based on the observed results, it was found that the $Al_4B_2O_9$ particles formed during the SHS are responsible for the low friction coefficient. The quantum chemical calculations showed that the elastic moduli of $Al_4B_2O_9$ are significantly smaller than the elastic moduli of $AlMgB_{14}$ and TiB_2. Thus, during sliding, $Al_4B_2O_9$ particles are squeezed out onto the composite surface, form the lubricating layer and reduce the friction coefficient.

Keywords: ceramics; DFT; tribo-layer; friction; tribology; nanohardness

Citation: Nikitin, P.; Zhukov, I.; Tkachev, D.; Abzaev, Y.; Marchenko, E.; Vorozhtsov, A. Experimental and Theoretical Study of Ultra-Hard $AlMgB_{14}$-TiB_2 Composites: Structure, Hardness and Self-Lubricity. *Materials* **2022**, *15*, 8450. https://doi.org/10.3390/ma15238450

Academic Editor: Hongyu Yang

Received: 17 October 2022
Accepted: 23 November 2022
Published: 27 November 2022

1. Introduction

Currently, $AlMgB_{14}$-based materials (BAMs) are of great interest due to their unique physical and mechanical properties. BAMs have an extremely low friction coefficient (COF, ~0.08–0.02) [1–3], a high hardness, with value reaching 32 GPa [4], a coefficient of thermal expansion (CTE) close to steel (11.7×10^{-6} K^{-1}) [5], and a high thermal and chemical stability. Although $AlMgB_{14}$ single crystals were first obtained in 1970 by Matkovich and Economy [6], polycrystalline materials based on $AlMgB_{14}$ have been actively studied since 2000 in the Ames Laboratory (USA) [2–4]. First, the scientists of [4] found that the addition of TiB_2 increases the hardness of the $AlMgB_{14}$-TiB_2 composite to 40–46 GPa, and then the studies of the tribological characteristics showed that the friction coefficient of the $AlMgB_{14}$ coating in dry conditions can reach 0.05 [3], while the friction coefficient of the $AlMgB_{14}$-TiB_2 coating in a water-glycol lubricant can reach values of 0.02 [1]. Due to the unique combination of these properties, $AlMgB_{14}$ has attracted great attention as a wear-resistant material in the friction units of critical machine parts.

Tribological analysis showed that the extremely low friction coefficient in dry conditions and water-glycol lubricants is associated with the release of B_2O_3 and $B(OH)_3$ particles [1–3] during the friction. Studies of the tribological characteristics of $AlMgB_{14}$-TiB_2 composites in dry conditions [7] revealed that the COF of $AlMgB_{14}$-30 wt% TiB_2 at room temperature varies in the range from 0.45 to 0.65 against the SiC counterface and decreases significantly to 0.2 at 800 °C. The authors of [7] attribute this effect to the formation of TiO_2 and B_2O_3 oxygen compounds on the contact surfaces of materials. Studies of the tribological characteristics of $AlMgB_{14}$-Si composites [8] have shown that the friction coefficient under dry conditions varies from 0.19 to 0.28 when sliding against the 316 L counterface. A low COF is associated with the release of Si particles onto the worn surface. A similar effect was observed in [9]: studies have shown that one of the reasons for the low friction coefficient (COF, 0.12) of Cu/$AlMgB_{14}$ composites is that $AlMgB_{14}$ particles are squeezed out of a rigid Cu matrix onto a worn surface under the action of external stress.

Based on the given data, it can be concluded that the low friction coefficient of various composites $AlMgB_{14}$-X (X = TiB_2, Si, Cu) corresponds to the release of certain particles on the surface of the material during friction. These particles lubricate the surface, reducing the COF and wear, respectively. They are released either in the rigid metal matrix [8,9], or when using certain lubricants [1–3], or when the surface is heated [7]. At the same time, the question of the mechanism of the self-lubrication of bulk composites $AlMgB_{14}$-TiB_2 in dry conditions at room temperature remains open.

In this work, the $AlMgB_{14}$-TiB_2 precursor was produced using a cost-effective technology of self-propagating high-temperature synthesis (SHS) [10]. Thereafter, the bulk $AlMgB_{14}$-TiB_2 composite was fabricated using the spark plasma sintering (SPS) method. The mechanism of the self-lubricity, phase composition, structure and properties of the obtained $AlMgB_{14}$-TiB_2 composite were studied.

2. Materials and Methods

2.1. Materials Preparation

To obtain the $AlMgB_{14}$-TiB_2 precursor, a simple and low-cost technology of SHS was used. (Ti + 2B) exothermic mixture was chosen as the donor component. For this, 69 wt% of titanium was mixed with 31 wt% of boron. The mixture of an intermetallic alloy $Al_{12}Mg_{17}$ (the process of obtaining the $Al_{12}Mg_{17}$ powder is described in detail in [11] and amorphous boron powder) was used as an acceptor mixture. For this, $Al_{12}Mg_{17}$ powder was mixed with B powder in the ratio of 25 wt% $Al_{12}Mg_{17}$–75 wt% B. The characteristics of the raw precursors are given in Table 1. The obtained powders were mixed in the ratio of 50 wt% ($Al_{12}Mg_{17}$: B)–50 wt% (Ti + 2B). The mixing was carried out in ethanol. After drying in a vacuum furnace at 200 °C for 4 h, a sample was prepared from the obtained mixture, which was then synthesized by the SHS method. The process of obtaining $AlMgB_{14}$-TiB_2 precursors by SHS is described in detail in [10].

Table 1. Characteristics of the raw powders.

Raw Precursors	Particle Size, μm	Purity, %
Ti	140	≥99.2
Amorphous B	0.6	≥98.7
$Al_{12}Mg_{17}$	15	≥99.2

In the second set, the produced $AlMgB_{14}$-TiB_2 precursor was consolidated and sintered by spark plasma sintering (DR. SINTER model SPS-625 Spark Plasma Sintering System, SPS SYNTEX INC. Ltd., Tokyo, Japan) in a 12.8 mm graphite die in an argon atmosphere. The sintering temperature was 1500 °C (the heating rate was 50 °C/min without holding time). The pressure was 70 MPa. The diameter and thickness of the obtained composite were ~12.5 mm and 3 mm, respectively. After sintering, the sample was taken out from the die, and the surface of the sample was polished with diamond pastes (the maximum surface roughness was 0.5 μm).

2.2. Measurements

The combustion temperature was measured using a tungsten-rhenium thermocouple (Promelectronica, Yekaterinburg, Russia). The morphology, elemental composition and grain size of the $AlMgB_{14}$-TiB_2 precursor were observed by scanning electron microscopy (JEOL JSM-6490, JEOL, Tokyo, Japan) at BEC (backscattered electron) and MIX (backscattered electron + secondary electron) modes equipped with an energy dispersive spectroscopy (EDX). To determine the amount of oxygen in the initial powders, a LECO ONH (St. Joseph, MI, USA) analyser was used. X-ray structural studies of the $AlMgB_{14}$-TiB_2 composite material were carried out on a Shimadzu 7000 (Kyoto, Japan) diffractometer. The phase composition was refined using the Rietveld method with the Diffrac.EVA program and Powder Diffraction File database. The theoretical XRD pattern was obtained by combining three reference XRD patterns of $AlMgB_{14}$, TiB_2 and $Al_4B_2O_9$ phases. The CASTEP program code [12,13] was used to calculate the free energies (E) of the reference and refined crystal lattices within the framework of the density functional theory (DFT) using the generalized-gradient approximation (GGA). Ultrasoft pseudopotentials were used, and the cutoff energy was 500 eV. The density of the $AlMgB_{14}$-TiB_2 composite was calculated by Archimedes' principle in distilled water. The nanohardness was measured using a benchtop nanoindentation system (CSM Instruments— Peseux, Switzerland). The load was 300 mN, and the holding time was 10 s. The determination of the nanohardness was carried out by the methods of Oliver and Pharr [14]. The Berkovich indenter was used in the work. The obtained nanohardness results were converted into Vickers microhardness. The friction coefficient was measured on a pin-on-disk tribometer (TRIBOTester, TRIBOtechnic, San Francisco, CA, USA). Al_2O_3 ball was used as a counter-specimen. The normal load was 5 N, and the speed was 25 mm/s with the test duration of 1500 s. The tests were performed under normal conditions at room temperature in air without using a lubricant coating. The topographic and energy dispersive (EDX) analysis of the near-surface regions of the sample after the sliding friction was performed on a Tescan Mira 3 (TESCAN, Brno, Czech Republic) scanning microscope.

3. Results

3.1. Combustion Temperature and Morphology of the $AlMgB_{14}$-TiB_2 Precursor

The results of measuring the temperature (the heat pattern is given in the Supplementary Materials) showed that during the exothermic reaction (Ti + 2B), the temperature increases to 1980 °C, and titanium diboride grains are formed. The heat released during the reaction is spent on the reaction in the $Al_{12}Mg_{17}$:B acceptor mixture with the formation of $AlMgB_{14}$ [15]. According to the presented SEM images (Figure 1), the produced $AlMgB_{14}$-TiB_2 precursor consists of particles with an average size of 1 μm. EDX analysis (given in Supplementary Materials) showed that Ti and B elements were found in the light areas, which corresponds to the TiB_2 phase. The B, Al and Mg elements were found in the dark areas, which corresponds to the $AlMgB_{14}$ phase. The titanium diboride particles (light particles) also form agglomerates. The formation of TiB_2 agglomerates is due to the fact that the heat released during the reaction (Ti + 2B) also leads to the fusion of TiB_2 grains [16,17].

3.2. Phase Composition of the $AlMgB_{14}$-TiB_2 Composite

The results of the XRD analysis of the spark plasma sintered $AlMgB_{14}$-TiB_2 composite are shown in Figure 2. The results of the X-ray structural analysis are shown in Table 2 (a, b, c, α, β, γ are the structural parameters, V is the volume of the crystal lattices and E is the free energy of crystal lattices of the detected phases). The analysis of the contributions to the integral intensity of the individual phases (Table 2, Figure 2) showed that the main phases are TiB_2, $AlMgB_{14}$, and $Al_4B_2O_9$.

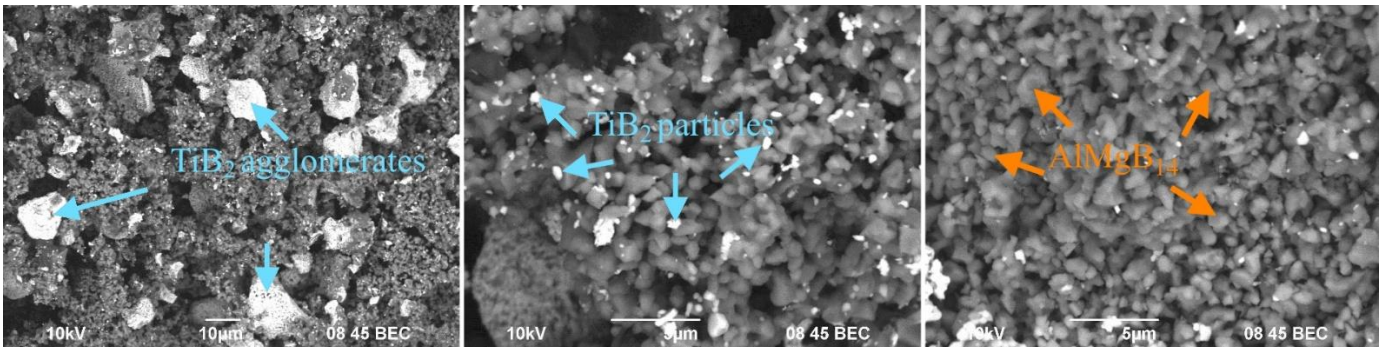

Figure 1. SEM images of the $AlMgB_{14}$-TiB_2 precursor (backscattered electron).

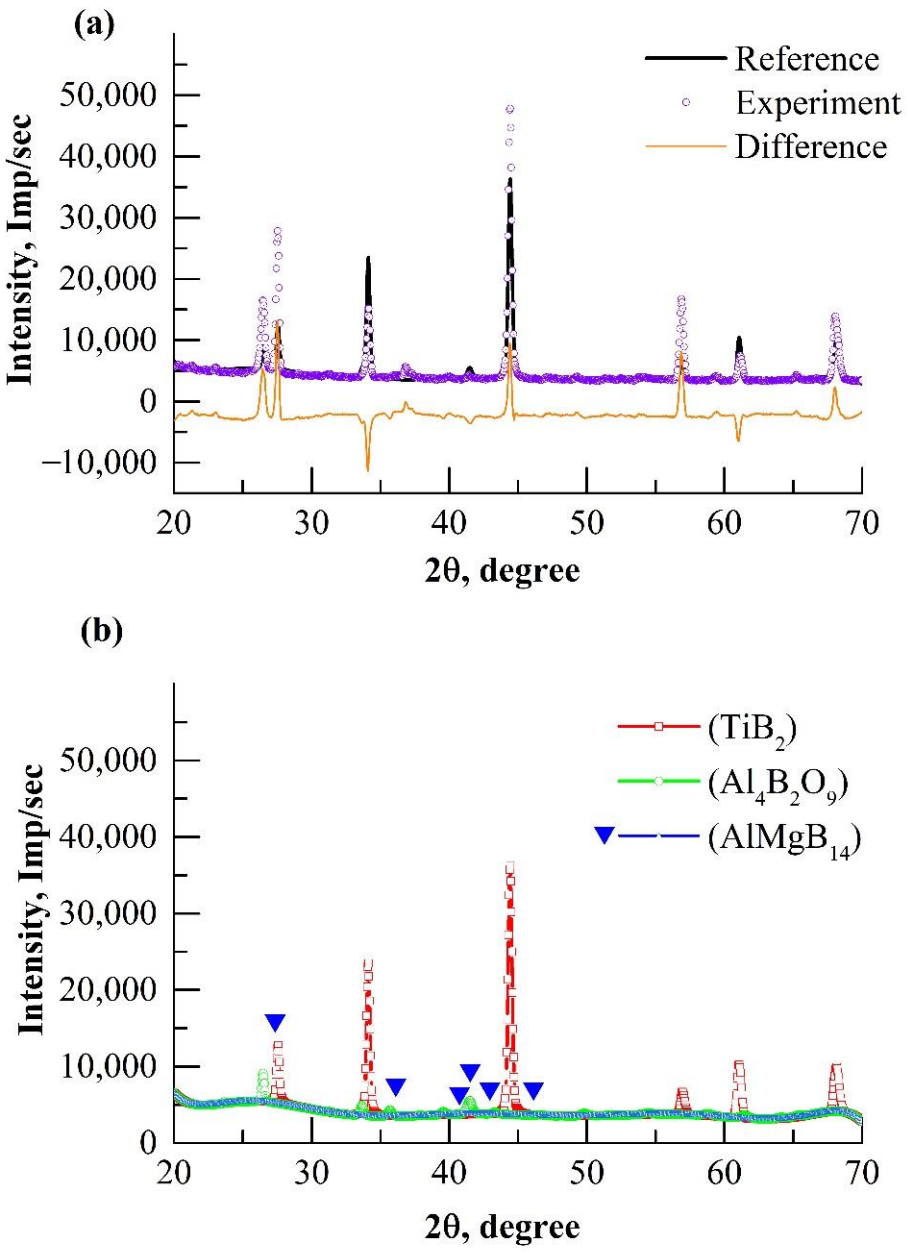

Figure 2. XRD patterns of the spark plasma sintered $AlMgB_{14}$-TiB_2 composite: (**a**) reference and experimental XRD patterns; (**b**) XRD patterns of the phases, found by the Rietveld method.

Table 2. Structural parameters of the detected phases.

Phase	State	a, Å	b, Å	c, Å	α = β	γ	V, Å^3	E, eV
TiB_2	Reference	3.009	3.009	3.262	90.00	120.00	25.578	−210.90
	Refined	3.033	3.033	3.240	90.00	120.00	25.816	−210.89
$AlMgB_{14}$	Reference	5.848	8.115	10.313	90.00	90.00	489.419	−7149.38
	Refined	5.690	8.050	10.357	90.00	90.00	474.448	−7148.67
$Al_4B_2O_9$	Reference	14.792	15.028	5.534	90.00	90.96	1230.15	−34471.7
	Refined	14.460	15.036	5.475	90.00	85.51	1152.61	−34469.3

The experimental XRD pattern of the obtained composite is well approximated by the calculated integral intensity (Figure 2a). The refined parameters of the main phases slightly differ from the reference. According to the results obtained using the light element analyzer LECO ONH, the main source of oxygen for the formation of the $Al_4B_2O_9$ oxide phase is boron powder (the oxygen content is 1.1 wt%).

3.3. Microstructure of the $AlMgB_{14}$-TiB_2 Composite

The microstructure of the fracture surface and the near-surface region of the spark plasma-sintered $AlMgB_{14}$-TiB_2 composite are shown in Figure 3. The structure of the obtained composite is not uniform. According to the EDX results, the Ti and B elements were found in the light areas (should be TiB_2 phase). In the dark areas, the B, Al and Mg elements were found in the ratio corresponding to the $AlMgB_{14}$ phase. $AlMgB_{14}$ grains have an average size of 3–5 μm, while the TiB_2 grains have an average size of 1–3 μm. The structure of the composite also contains large agglomerates of TiB_2, which are formed from agglomerates in the $AlMgB_{14}$-TiB_2 precursor [18].

3.4. Hardness and Density of the $AlMgB_{14}$-TiB_2 Composite

According to the nanohardness measurement results, in the areas corresponding mainly to $AlMgB_{14}$, the average Vickers microhardness is 32.5 GPa. In the regions corresponding to TiB_2, the average Vickers microhardness hardness is 33.1 GPa. In the $AlMgB_{14}$-TiB_2 interlayer, the average hardness of the sample is 37.4 GPa with a maximum detected hardness value of 44.1 GPa. The obtained results are similar to the results of other authors (Table 3) [4,7,19,20]. The density of the obtained sample is 3.271 g/cm^3 at a theoretical density of 3.29 g/cm^3 (pure 50 wt% of TiB_2 + 50 wt% of $AlMgB_{14}$ composite).

Table 3. Comparison of hardness values of $AlMgB_{14}$-based materials.

Composition	Hardness Value, GPa	Reference
$AlMgB_{14}$ + 50 wt% TiB_2	40–46	[4]
$AlMgB_{14}$ + 30 wt% Si	27	[8]
$AlMgB_{14}$-5Al	22.4	[21]
$AlMgB_{14}$	26.7	[22]
$AlMgB_{14}$ + 50 wt% TiB_2	37.4	This work

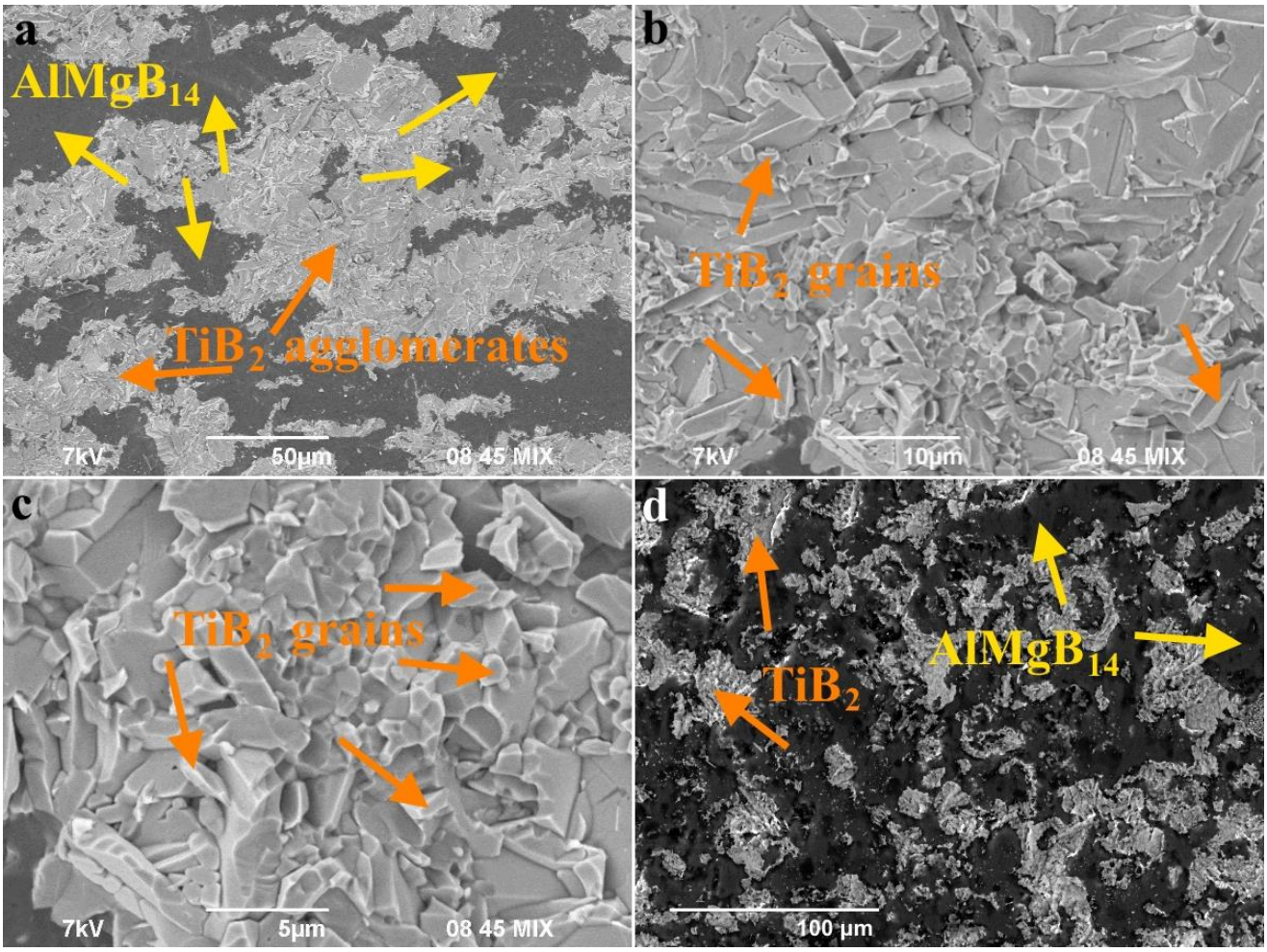

Figure 3. SEM images of the fracture surface (**a**–**c**) and the surface (**d**) of the $AlMgB_{14}$-TiB_2 composite.

3.5. Tribological Behavior of the $AlMgB_{14}$-TiB_2 Composite

Figure 4 shows the curve of the change in the friction coefficient of the obtained $AlMgB_{14}$-TiB_2 composite. To compare this result, we also measured the friction coefficient of the $AlMgB_{14}$ and 30 wt% TiB_2 samples obtained in our previous works [10,23]. It was found that the friction curve of the obtained $AlMgB_{14}$-TiB_2 sample has a downward trend, while the curves of the $AlMgB_{14}$ and $AlMgB_{14}$-TiB_2 samples, on the contrary, have an upward trend. Moreover, the change in the values of the friction coefficient of the obtained $AlMgB_{14}$-TiB_2 composite has an atypical character in comparison with other samples: as can be seen from Figure 4, two extrema were found in the range of the COF values of 0.35 and 0.4, respectively. After reaching the value of 0.4, the friction coefficient sharply decreases to a value of 0.18, increases to 0.22 and decreases linearly to 0.18. At the same time, according to the XRD results, in contrast to the $AlMgB_{14}$ [23] and $AlMgB_{14}$–30 wt% TiB_2 [10] samples, the $Al_4B_2O_9$ phase was found in the obtained composite. A similar result was observed in [7], where due to the plastic deformation and elevated temperature TiO_2 particles formed a lubrication layer. Thus, it can be assumed that during friction, the friction coefficient increases until some particles (presumably, $Al_4B_2O_9$) appear on the surface of the sample and form a lubricating coating. After that, a decrease in the friction coefficient is observed.

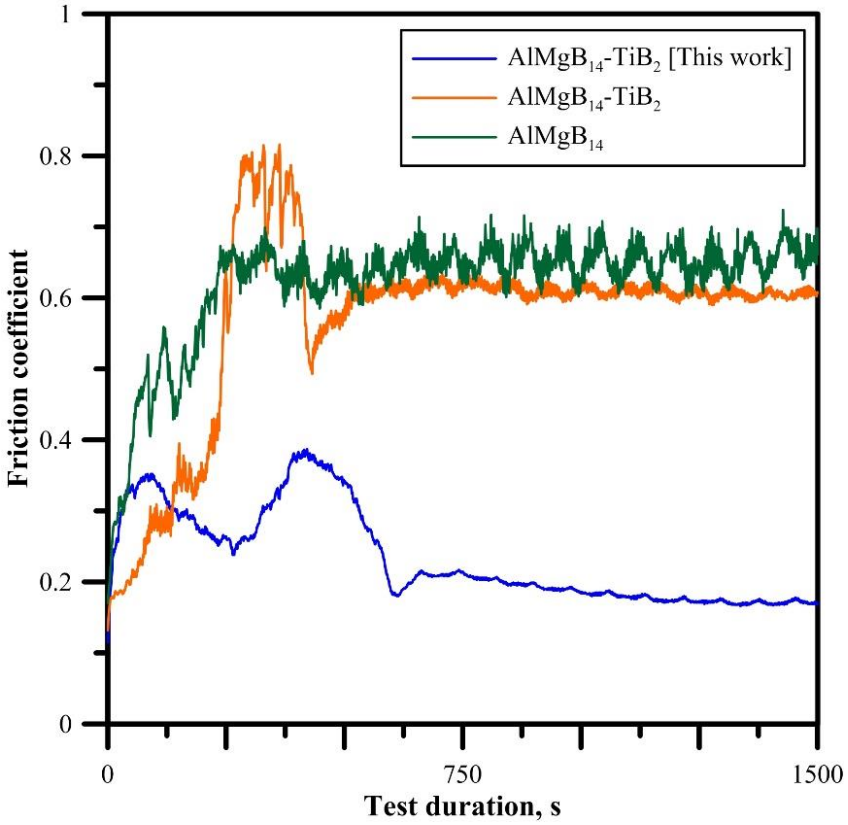

Figure 4. Friction coefficient of the obtained $AlMgB_{14}$-TiB_2 composite under dry conditions.

4. Discussion

4.1. Formation of the $Al_4B_2O_9$ Phase

According to the XRD results (Table 2), the $Al_4B_2O_9$ phase was found in the obtained $AlMgB_{14}$-TiB_2 composite. It is known that the optimum temperature for obtaining $AlMgB_{14}$-based materials is 1400 °C [4]. In work [24], a mechanism for the decomposition of $AlMgB_{14}$ during spark plasma sintering was proposed. It was found that, upon the local overheating of the powder mixture (1470 °C) during spark plasma sintering, $AlMgB_{14}$ decomposes and the decomposition products react with $MgAl_2O_4$ spinel, forming the $Al_4B_2O_9$ borate. In this work, the overheating of the powder mixture was also observed both during the preparation of the $AlMgB_{14}$-TiB_2 precursor (the synthesis temperature was 1980 °C) and during the fabrication of the $AlMgB_{14}$-TiB_2 composite (the sintering temperature was 1500 °C). It should also be noted that the main impurity phase $MgAl_2O_4$ [4] was not detected in the $AlMgB_{14}$-TiB_2 composite. Thus, it is confirmed that $AlMgB_{14}$ decomposes and reacts with $MgAl_2O_4$, forming aluminum borate $Al_4B_2O_9$, during SHS and SPS due to local overheating.

4.2. Structure and Phase Composition of the $AlMgB_{14}$-TiB_2 Composite

The crystalline phases of TiB_2 and $AlMgB_{14}$ are precipitated in the composite material. Indeed, quantitative phase analysis (Table 2, Figure 2b) showed that the contribution of the intensity of the TiB_2 lattice (Figure 2b, mark 4) is dominant in the crystalline part of the integrated intensity (Figure 2a, mark 2). For these phases, complete structural information was found (Table 2). An increase in the lattice parameters was found, but the volume of the $AlMgB_{14}$ crystal lattice decreased relative to the reference, which is associated with a change in the shape of the lattice.

Complete information about the structure makes it possible to elucidate from the first principles the stability of the lattices of the main phases of the $AlMgB_{14}$-TiB_2 composite. The details of the calculations are given in Section 4.3. The estimates from the first principles

showed that the lattice energies of the main phases (TiB_2, $AlMgB_{14}$ and $Al_4B_2O_9$) are negative; therefore, they are stable (Table 2). The $Al_4B_2O_9$ supercell is also stable to the lattice separation of the Al_2O_3 and B_2O_3 phases (Section 4.3). Indeed, its binding energy is $|\Delta Est| \approx 2163$ eV. The analysis of the morphology of the fracture surface (Figure 3a–c) showed that TiB_2 agglomerates (light areas) are characterized by a clear separation of interfaces between crystallites of various shapes and sizes with an arbitrary direction, while $AlMgB_{14}$ (dark areas), on the contrary, are characterized by a blurred surface relief (Figure 3c).

4.3. Mechanism of Self-Lubricity of the $AlMgB_{14}$-TiB_2 Composite

An analysis of the literature data [7–9] shows that the nature of the change in the friction coefficient under the dry conditions of the obtained $AlMgB_{14}$-TiB_2 composite is not typical for $AlMgB_{14}$ materials and $AlMgB_{14}$-TiB_2 composite materials (Figure 4). Thus, of particular interest are studies aimed at identifying the mechanism for reducing the friction coefficient in the obtained composite. Since the $Al_4B_2O_9$ lattice is a supercell with the chemical formula $\{2(Al_2O_3) \times (B_2O_3)\}$ (that is, it contains B_2O_3 particles in its compound, which are responsible for the lubrication of $AlMgB_{14}$-TiB_2 composite materials [2]), it is assumed that the dry friction process is significantly influenced by B_2O_3 particles, as well as the morphology of $AlMgB_{14}$.

To reveal the mechanism of self-lubrication of the obtained $AlMgB_{14}$-TiB_2 composite, the stability of the $Al_4B_2O_9$ phase was calculated. Since $Al_4B_2O_9$ is a supercell with the chemical formula $\{2(Al_2O_3) \times (B_2O_3)\}$ (Figure 5), its stability ΔEst can be estimated by Formula (1):

$$\Delta E_{st} = \Delta E_{Al_4B_2O_9} - (x\Delta E_{Al_2O_3} + y\Delta E_{B_2O_3}) \quad (1)$$

where $\Delta Est < 0$ and x and y are the relative contents of the Al_2O_3 and B_2O_3 phases in the $Al_4B_2O_9$ supercell. $\Delta E_{Al_4B_2O_9}$ is the supercell energy. The lattice energies of the Al_2O_3 and B_2O_3 phases were calculated from the first principles and were $\Delta E_{Al_2O_3} = -8590.47$ eV and $\Delta E_{B2O3} = -4243.67$ eV. The lattice energy of $Al_4B_2O_9$ is given in Table 2, and the coefficients are: x = 16/6, y = 8/3. The estimates showed that $\Delta Est \approx -2163$ eV, demonstrating that the $Al_4B_2O_9$ lattice is substantially stable.

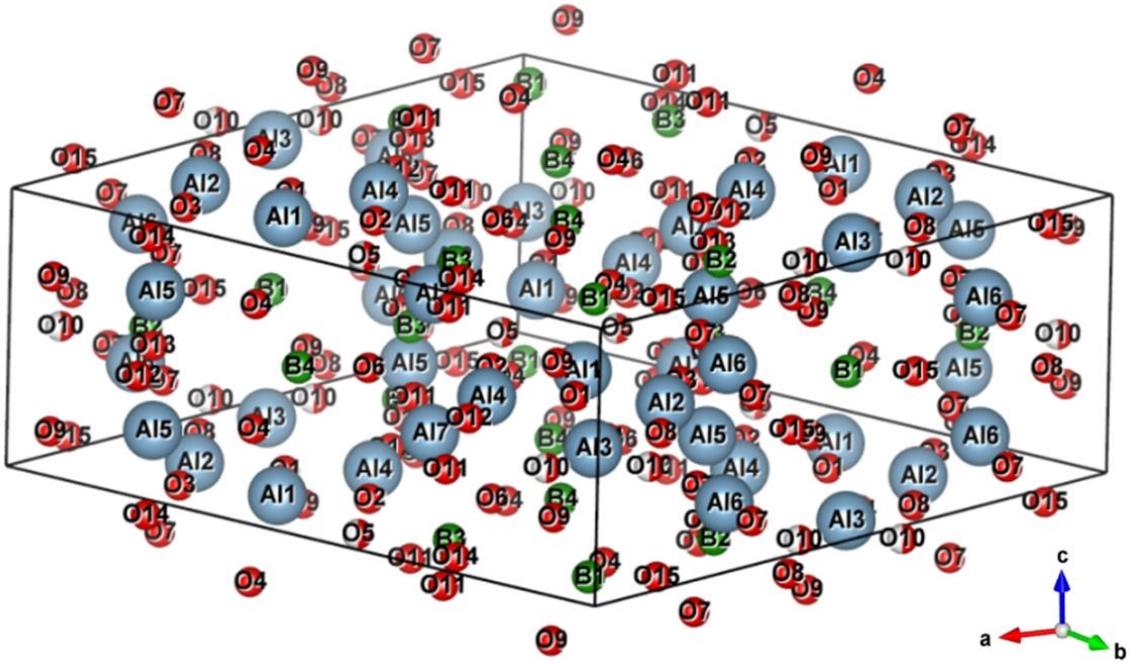

Figure 5. 3D image of the $Al_4B_2O_9$ lattice after refinement of structural parameters by the Rietveld method.

In the next stage, quantum-chemical calculations of the elastic moduli of the main phases were performed using the method [25,26]. The results are given in Table 4. The obtained results are in a good agreement with the experimentally observed value. The elastic lattice moduli of $Al_4B_2O_9$ are significantly smaller than those of TiB_2 and $AlMgB_{14}$. It should also be noted that the elastic moduli of the $AlMgB_{14}$ are less than the corresponding values of TiB_2; $AlMgB_{14}$ can be a "viscous" base of the composite during the dry friction. Thus, it is assumed that the $Al_4B_2O_9$ particles are squeezed out of the rigid TiB_2 matrix and viscous $AlMgB_{14}$ matrix onto the composite surface and lubricate it, which leads to a decrease in the friction coefficient.

Table 4. Elastic moduli (GPa) of the main phases of the obtained material.

Phase	Young's Modulus	Young's Modulus (Experimental Value) *	Bulk Modulus	Shear Modulus
TiB_2	491.8		245.9	210.8
$AlMgB_{14}$	424.7	480.1	237.3	182.9
$Al_4B_2O_9$	206.2		132.0	83.2

*—From nanohardness measurements.

To find particles of the $Al_4B_2O_9$ composition on the surface and thus prove this hypothesis, the elemental composition of the EDX method was determined in the track region. Figure 6 shows a fragment of the topographic surface of the $AlMgB_{14}$-TiB_2 composite in the track region after measuring the friction coefficient.

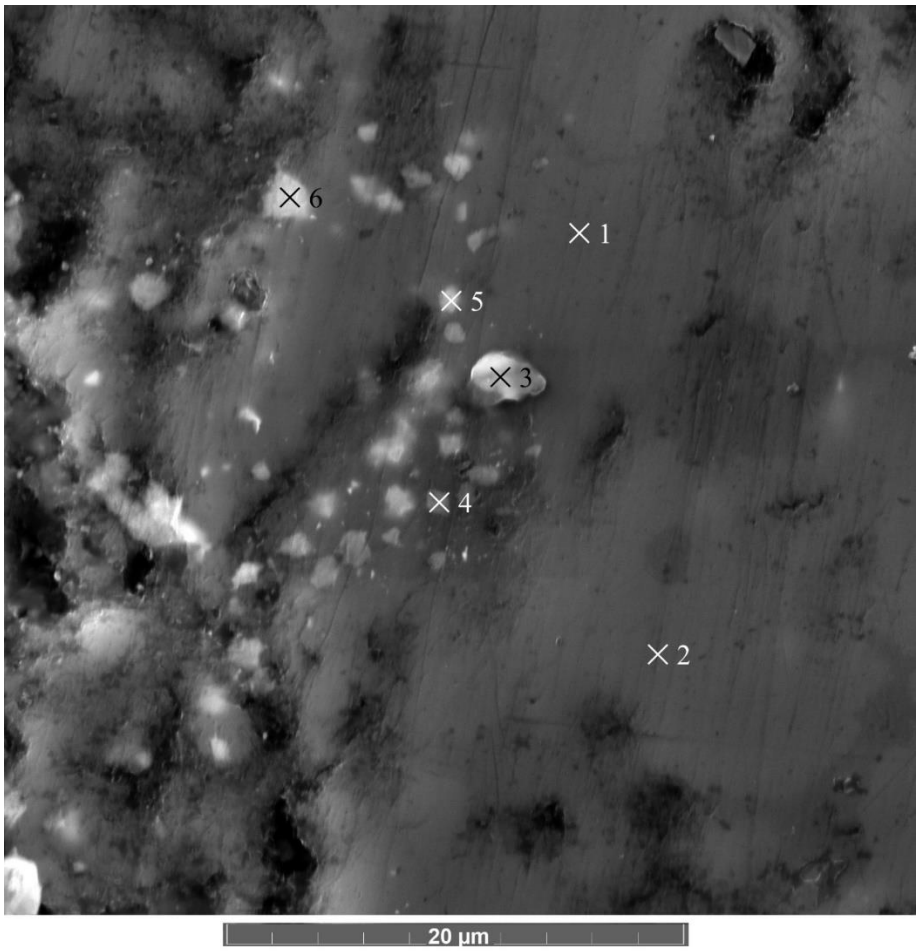

Figure 6. SEM image of the relief of the $AlMgB_{14}$-TiB_2 composite after friction testing (on the surface, the areas where the elemental composition is determined are marked).

The mass fraction of the elements in the corresponding regions is given in Table 5. The results of the estimates of the molar fraction indicate that in spectra 3, 4, 5 and 6 (Figure 6), the areas of destruction of the $Al_4B_2O_9$ particles as a result of the sliding friction with the release of the B_2O_3 and Al_2O_3 compounds of a variable composition are found.

Table 5. Spectra of elements in selected places on the surface of the $AlMgB_{14}$-TiB_2 composite.

Element	Mark 1	Mark 2	Mark 3	Mark 4	Mark 5	Mark 6
	wt%					
B	84.4	93.1	66.7	49.0	55.8	43.9
Al	8.8	8.5	8.7	17.7	15.0	20.9
Mg	6.1	6.0	5.9	9.3	7.5	9.7
Ti	0.4	2.1	0.4	0.4	0.3	0.3
O	–	0.2	18.3	23.5	21.3	25.1
Estimated phase	$AlMgB_{14}$	$AlMgB_{14}/TiB_2$	$Al_4B_2O_9$	$Al_4B_2O_9$	$Al_4B_2O_9$	$Al_4B_2O_9$

Thus, $Al_4B_2O_9$ particles are distributed on the surface of a sample consisting of a rigid TiB_2 matrix with a "viscous" base of the $AlMgB_{14}$ (spectra 1 and 2) phase.

As previously reported in the Introduction, the effect of squeezing out particles onto the surface of $AlMgB_{14}$-based materials was observed in other studies. A comparison of the friction coefficients is shown in Table 6. In [27,28], it was found that in the Al_2O_3-TiB_2 composites, during friction at elevated temperatures in the air, an oxide layer is formed, which lubricates the sample. In turn, the formation of the oxide layer is due to the plastic deformation of the tribo-contact region and the fact that the critical shear modulus of the oxide layer is much less than the shear modulus of the substrate. In this work, similar results were obtained: a sharp decrease in the COF is associated with the release of B_2O_3 and Al_2O_3 particles of a variable composition from the rigid TiB_2 matrix with the "viscous" base of the $AlMgB_{14}$ phase onto the composite surface during friction. These particles form a lubricating tribolayer and reduce the friction coefficient. In other words, the effect of the self-lubrication of the surface of the composite material $AlMgB_{14}$-TiB_2 with $Al_4B_2O_9$ particles is observed.

Table 6. Comparison of friction coefficients in dry conditions of the $AlMgB_{14}$-based materials.

Composition	Friction Coefficient	Reason of Low COF	Reference
$AlMgB_{14}$	0.38	–	[11]
$AlMgB_{14}$-TiB_2	0.45–0.65	–	[7]
$AlMgB_{14}$-TiB_2	0.12 (800 °C)	TiO_2 particles	[7]
$AlMgB_{14}$-Si	0.19–0.28	316L counter-specimen Si particles	[8]
$AlMgB_{14}$-Cu	0.2	$AlMgB_{14}$ particles	[9]
$AlMgB_{14}$-TiB_2	0.18	$Al_4B_2O_9$ particles	This work

Thus, the $Al_4B_2O_9$ additive can be used as a lubricant in $AlMgB_{14}$-TiB_2 composite materials under dry friction conditions. It should be noted that according to the presented results, $Al_4B_2O_9$ does not negatively affect the hardness of the $AlMgB_{14}$-TiB_2 composite system. In the future, of particular interest is the study of $AlMgB_{14}$-TiB_2 composite materials that use prereacted $Al_4B_2O_9$ as the initial precursor.

5. Conclusions

1. The $AlMgB_{14}$-TiB_2 composite was spark plasma sintered from the SHS precursor.
2. The main phases in the obtained composite are TiB_2, $AlMgB_{14}$ and $Al_4B_2O_9$.
3. The maximum hardness of the composite is 44.1 GPa at a density of 3.271 g/cm^3.
4. The presence of oxygen in the form of the $Al_4B_2O_9$ phase led to unexpectable results: the friction coefficient of the obtained $AlMgB_{14}$-TiB_2 composite in dry conditions

against the Al_2O_3 counter-specimen is 0.18. It is approximately four times lower than the friction coefficient of pure ceramic $AlMgB_{14}$ (COF, 0.7).

5. It was found that $Al_4B_2O_9$ particles are responsible for the low friction coefficient: the elastic moduli of $Al_4B_2O_9$ are significantly smaller than the elastic moduli of $AlMgB_{14}$ and TiB_2. Thus, during the friction, due to the plastic deformation of the tribo-contact region, $Al_4B_2O_9$ particles are squeezed out onto the composite surface, form the lubricating layer and reduce the friction coefficient.

Supplementary Materials: The following supporting information can be downloaded at: https://www.mdpi.com/article/10.3390/ma15238450/s1. Figure S1: Heat pattern of the SHS process. Figure S2: EDX_results to Figure 1. Figure S3: Nanohardness indentations.

Author Contributions: Conceptualization, P.N. and Y.A.; investigation, P.N., I.Z., D.T., Y.A. and E.M.; writing—original draft preparation, P.N.; writing—review and editing, P.N., D.T. and I.Z.; visualization—P.N. and Y.A.; funding acquisition—I.Z.; resources—I.Z. and A.V. All authors have read and agreed to the published version of the manuscript.

Funding: These studies were funded by the Russian Science Foundation (project No. 19-79-10042).

Data Availability Statement: The data presented in this study are available in the article.

Acknowledgments: The SEM researches were carried out with the equipment of Tomsk Regional Core Shared Research Facilities Center of National Research Tomsk State University (Grant of the Ministry of Science and Higher Education of the Russian Federation no. 075-15-2021-693 (no. 13.RFC.21.0012)).

Conflicts of Interest: The authors declare no conflict of interest.

References

1. Lu, X.; Yao, K.; Ouyang, J.; Tian, Y. Tribological characteristics and tribo-chemical mechanisms of Al–Mg–Ti–B coatings under water–glycol lubrication. *Wear* **2015**, *326*, 68–73. [CrossRef]
2. Cook, B.A.; Harringa, J.L.; Anderegg, J.; Russell, A.M.; Qu, J.; Blau, P.J.; Elmoursi, A.A. Analysis of wear mechanisms in low-friction $AlMgB_{14}$–TiB_2 coatings. *Surf. Coat. Technol.* **2010**, *205*, 2296–2301. [CrossRef]
3. Tian, Y.; Bastawros, A.F.; Lo, C.C.; Constant, A.P.; Russell, A.M.; Cook, B.A. Superhard self-lubricating $AlMgB_{14}$ films for microelectromechanical devices. *Appl. Phys. Lett.* **2003**, *83*, 2781–2783. [CrossRef]
4. Cook, B.A.; Harringa, J.L.; Lewis, T.L.; Russel, A.M. A new class of ultra-hard materials based on $AlMgB_{14}$. *Scr. Mater.* **2000**, *42*, 597–602. [CrossRef]
5. Russell, A.M.; Cook, B.A.; Harringa, J.L.; Lewis, T.L. Coefficient of thermal expansion of $AlMgB_{14}$. *Scr. Mater.* **2002**, *46*, 629–633. [CrossRef]
6. Matkovich, V.I.; Economy, J. Structure of $MgAlB_{14}$ and a brief critique of structural relationships in higher borides. *Acta Crystallogr. Sect. B Struct. Crystallogr. Cryst. Chem.* **1970**, *26*, 616–621. [CrossRef]
7. Lei, Y.; Meng, Q.; Zhuang, L.; Chen, S.; Hu, L.; Cheng, H. Friction and wear behavior of $AlMgB_{14}$–TiB_2 composite at elevated temperature. *Tribol. Lett.* **2014**, *56*, 435–442. [CrossRef]
8. Chen, J.; Cheng, J.; Li, F.; Zhu, S.; Li, W.; Yang, J.; Liu, W. Tribological study on a novel wear-resistant $AlMgB_{14}$-Si composite. *Ceram. Int.* **2017**, *43*, 12362–12371. [CrossRef]
9. Cheng, J.; Ma, J.; Li, F.; Qiao, Z.; Yang, J.; Liu, W. Dry-sliding tribological properties of Cu/$AlMgB_{14}$ composites. *Tribol. Lett.* **2014**, *55*, 35–44. [CrossRef]
10. Nikitin, P.Y.; Zhukov, I.A.; Matveev, A.E.; Sokolov, S.D.; Boldin, M.S.; Vorozhtsov, A.B. $AlMgB_{14}$–TiB_2 composite materials obtained by self-propagating high-temperature synthesis and spark plasma sintering. *Ceram. Int.* **2020**, *46*, 22733–22737. [CrossRef]
11. Zhukov, I.A.; Nikitin, P.Y.; Vorozhtsov, A.B.; Perevislov, S.N.; Sokolov, S.D.; Ziatdinov, M.H. The use of intermetallic Al_xMg_y powder to obtain $AlMgB_{14}$-based materials. *Mater. Today Commun.* **2020**, *22*, 100848. [CrossRef]
12. Clark, S.J.; Segall, M.D.; Pickard, C.J.; Hasnip, P.J.; Probert, M.I.; Refson, K.; Payne, M.C. First principles methods using CASTEP. *Z. Kristallogr.-Cryst. Mater.* **2005**, *220*, 567–570. [CrossRef]
13. Evseev, N.S.; Matveev, A.E.; Nikitin, P.Y.; Abzaev, Y.A.; Zhukov, I.A. A theoretical and experimental investigation on the SHS synthesis of (HfTiCN)-TiB_2 high-entropy composite. *Ceram. Int.* **2022**, *48*, 16010–16014. [CrossRef]
14. Oliver, W.C.; Pharr, G.M. An improved technique for determining hardness and elastic modulus using load and displacement sensing indentation experiments. *J. Mater. Res.* **1992**, *7*, 1564–1583. [CrossRef]
15. Nikitin, P.Y.; Matveev, A.E.; Zhukov, I.A. Energy-effective $AlMgB_{14}$ production by self-propagating high-temperature synthesis (SHS) using the chemical furnace as a source of heat energy. *Ceram. Int.* **2021**, *47*, 21698–21704. [CrossRef]

16. Matveev, A.E.; Zhukov, I.A.; Ziatdinov, M.H.; Zhukov, A.S. Planetary Milling and Self-Propagating High-Temperature Synthesis of Al-TiB_2 Composites. *Materials* **2020**, *13*, 1050. [CrossRef]
17. Matveev, A.; Promakhov, V.; Nikitin, P.; Babaev, A.; Vorozhtsov, A. Effect of Mechanical Activation of Al-Ti-B Powder Mixture on Phase Composition and Structure of Al-TiB_2 Composite Materials Obtained by Self-Propagating High-Temperature Synthesis (SHS). *Materials* **2022**, *15*, 2668. [CrossRef]
18. Nikitin, P.; Zhukov, I.; Matveev, A.; Sokolov, S.; Grigoriev, M.; Vorozhtsov, A. On the Structure and Properties of $AlMgB_{14}$-TiB_2 Composites Obtained from SHS Powders by Spark Plasma Sintering. *Materials* **2021**, *14*, 5521. [CrossRef]
19. Ahmed, A.; Bahadur, S.; Cook, B.A.; Peters, J. Mechanical properties and scratch test studies of new ultra-hard $AlMgB_{14}$ modified by TiB2. *Tribol. Int.* **2006**, *39*, 129–137. [CrossRef]
20. Kevorkijan, S.D.; Škapin, M.; Jelen, K.; Krnel, A. Meden, Cost-effective synthesis of $AlMgB_{14}$–xTiB_2. *J. Eur. Ceram. Soc.* **2007**, *27*, 493–497. [CrossRef]
21. Jiang, J.; Xie, J.; Zhong, H.; Dong, F.; Liu, N.; Tang, W.; Zhu, H.; Zhang, J. Synthesis and mechanical properties of $AlMgB_{14}$–Al composite. *J. Alloys Compd.* **2020**, *818*, 152910. [CrossRef]
22. Xie, Z.; DeLucca, V.; Haber, R.A.; Restrepo, D.T.; Todd, J.; Blair, R.G.; Orlovskaya, N. Aluminum magnesium boride: Synthesis, sintering and microstructure. *Adv. Appl. Ceram.* **2017**, *116*, 341–347. [CrossRef]
23. Nikitin, P.Y.; Zhukov, I.A.; Boldin, M.S.; Perevislov, S.N.; Chuvil'deev, V.N. Spark plasma sintering, phase composition, and properties of $AlMgB_{14}$ ceramic materials. *Rus. J. Inorg. Chem.* **2021**, *66*, 1252–1256. [CrossRef]
24. Nikitin, P.Y.; Zhukov, I.A.; Vorozhtsov, A.B. Decomposition mechanism of $AlMgB_{14}$ during the spark plasma sintering. *J. Mater. Res. Technol.* **2020**, *11*, 687–692. [CrossRef]
25. Mazhnik, E.; Oganov, A.R. Application of machine learning methods for predicting new superhard materials. *J. Appl. Phys.* **2020**, *128*, 075102. [CrossRef]
26. Mazhnik, E.; Oganov, A.R. A model of hardness and fracture toughness of solids. *J. Appl. Phys.* **2019**, *126*, 125109. [CrossRef]
27. Jianxin, D.; Xing, A.; Zhaoqian, L. Friction and wear behavior of Al_2O_3/TiB_2 composite against cemented carbide in various atmospheres at elevated temperature. *Wear* **1996**, *195*, 128–132. [CrossRef]
28. Jianxin, D.; Tongkun, C.; Lili, L. Self-lubricating behaviors of Al_2O_3/TiB_2 ceramic tools in dry high-speed machining of hardened steel. *J. Eur. Ceram. Soc.* **2005**, *25*, 1073–1079. [CrossRef]